The orbital structure and potential of NGC 1399

R.P. Saglia [1], Andi Kronawitter [2], Ortwin Gerhard [2,3], Ralf Bender [1]

ABSTRACT

Accurate and radially extended stellar kinematic data reaching $R = 97''$ from the center are presented for the cD galaxy of Fornax, NGC 1399. The stellar rotation is small (≤ 30 km/s); the stellar velocity dispersion remains constant at 250-270 km/s. The deviations from Gaussian line of sight velocity distributions are small, at the percent level.

We construct dynamical models of the galaxy, deprojecting its nearly round (E0-E1) surface brightness distribution, and determining the spherical distribution function that best fits (at the 4 percent level) the kinematic data on a grid of parametrized potentials. We find that the stellar orbital structure is moderately radial, with $\beta = 0.3 \pm 0.1$ for $R \leq 60''$, similar to results found for some normal giant ellipticals. The gravitational potential is dominated by the luminous component out to the last data point, with a mass-to-light ratio $M/L_B = 10$ $M_\odot/L_\odot$, although the presence of a central black hole of $M \approx 5 \times 10^8 M_\odot$ is compatible with the data in the inner 5 arcsec. The influence of the dark component is marginally detected starting from $R \approx 60''$. Using the radial velocities of the globular clusters and planetary nebulae of the galaxy we constrain the potential more strongly, ruling out the self-consistent case and finding that the best fit solution agrees with X-ray determinations. The resulting total mass and mass–to–light ratio are $M = 1.2 - 2.5 \times 10^{12} M_\odot$ and $M/L_B = 22 - 48$ $M_\odot/L_\odot$ inside $R = 417''$ or 35 kpc for D=17.6 Mpc.

Subject headings: line: profiles - celestial mechanics, stellar dynamics - galaxies: elliptical and lenticular, cD - galaxies: individual: NGC 1399 - galaxies: kinematics and dynamics - dark matter.

---

[1]Institut für Astronomie und Astrophysik, Scheinerstraße 1, D-81679 Munich, Germany

[2]Astronomisches Institut, Universität Basel, Venusstrasse 7, CH-4102 Binningen, Switzerland

[3]Max-Planck-Institut für Astrophysik, Karl-Schwarzschild-Str. 1, D-85740 Garching, Germany

1. Introduction

Determining the gravitational potential of elliptical galaxies and the amount of dark matter present is a notoriously difficult problem. This stems from the absence of extended cold gas which could be used as dynamical tracer, and the unknown intrinsic shape and orbital structure (e.g., Saglia 1996 and references therein). Progress has been made in recent years thanks to improved observational data and dynamical modeling techniques.

On the one hand, we are now able to measure not only the stellar velocity and velocity dispersion profiles, but also the shape parameters of the line of sight velocity distributions with good accuracy (van der Marel and Franx 1993; Bender, Saglia and Gerhard 1994, hereafter BSG94; Carollo et al. 1995; Gerhard et al. 1998a, hereafter G+98; Statler and Smecker-Hane 1999). Such data contain information on the anisotropy and the gravitational potential (Gerhard 1993, Merritt 1993). On the other hand, algorithms based on Schwarzschild's (1979) orbit superposition technique (Rix et al. 1997; Cretton et al. 1999) or on the non-parametric reconstruction of the underlying distribution function (G+98; Matthias and Gerhard 1999) allow a detailed modeling of the data.

Up to now, only a limited number of ellipticals have been analyzed with these methods (Rix et al. 1997; G+98; Matthias and Gerhard 1999). Nevertheless, the following pattern appears to emerge from these studies. Out to 1-2 half-luminosity radii R_e these objects are moderately radially anisotropic, and they have a dark component which starts to dominate the dynamics at about $R > 1 - 2R_e$. This is consistent with previous studies of extended velocity dispersion profiles of ellipticals (Saglia, Bertin and Stiavelli 1992; Saglia et al. 1993), of the radial velocities of globular clusters (Mould et al. 1990; Grillmair et al. 1994; Cohen and Ryzhov 1997; Minniti et al. 1998, Kissler-Patig et al. 1998) and planetary nebulae (Arnaboldi et al. 1994, 1998; Hui et al. 1995); of the X-ray emission around ellipticals (Ikebe et al. 1996, Jones et al. 1997) and, more recently, the modeling of strong lensing systems (Romanowsky and Kochaneck 1999) and the statistics of galaxy-galaxy lensing (Geiger and Schneider 1998).

In this paper we apply the non-parametric distribution function reconstruction method to new, accurate and extended data of the Fornax cD galaxy NGC 1399, to explore whether the conclusions reached for normal ellipticals are valid also for the class of the most massive early-type galaxies. A preliminary description of the results can be found in Kronawitter et al. (1999). In the following we adopt a distance of 17.6 Mpc. NGC 1399 has been the subject of a number of dynamical studies in the past. Bicknell et al. (1989) analyzed the major axis velocity dispersion profile using the Jeans equations, concluding that a constant mass-to-light ratio model with little anisotropy is able to reproduce the data out to $\approx 85''$. More recently, Graham et al. (1998) reached the same conclusion using models based on $R^{1/n}$ luminosity profiles. X-ray observations indicate that the outer parts ($R > 120'' = 10.2$ kpc) are dominated by a dark halo which merges into the one of the Fornax cluster at around $R \approx 53$ kpc (Ikebe et al. 1996). However, the potential inside $R \approx 10$ kpc is little constrained due to the presence of a cooling flow (Rangarajan et al. 1995). The radial velocities of globular clusters and planetary nebulae (see references above) agree with these mass determinations.

The structure of the paper is as follows. We present the data in §2, where also the data reduction and the comparison with the literature are described and discussed. We review our dynamical modeling approach in §3 and discuss some modifications needed for the analysis of NGC 1399. Results are presented in §4, where the constraints from the absorption line data are combined with those from globular cluster and planetary nebulae radial velocities and X-ray data. Conclusions are drawn in §5.

2. Observations of NGC 1399

The observations were performed from the 6th to the 8th of December 1994, using EMMI and the NTT, in remote observing mode from Garching. The grating # 6 (13.5 Å/mm) was used in combination with the ESO CCD Tek #36 (2048^2 24 μm pixels, 0.268 arcsec/pixel) and a 3 arcsec wide slit, giving a FWHM spectroscopic resolution of 3.5 Å. The central wavelength was 5150 Å, giving 85 km/s σ_{instr} resolution; the spectral range (4826-5474 Å) covered the absorption lines Hβ, Mg and Fe. A 1.5 hour long spectrum was taken along the major axis of the galaxy (PA=110^0); additional 9 hours of integrations were taken parallel to the minor axis, shifting the slit 42 arcsec from the center. Numerous template stars were also observed, wiggled and trailed along the slit.

The standard reduction steps (bias subtraction,

flat fielding, cosmic ray removal, logarithmic wavelength calibration, sky subtraction) were performed under MIDAS. A sky subtraction better than 1 per cent was achieved. The analysis of the data was carried out using the FCQ method (Bender 1990) following BSG94 and G+98 . The spectra were rebinned along the spatial direction to obtain a nearly constant signal-to-noise ratio larger than 50 per resolution element. The effects of the continuum fitting and instrumental resolution were extensively tested by Monte Carlo simulations. The residual systematic effects on the values of the h_3 and h_4 profiles are less than 0.01, and less than 1.5% in σ. The errorbars (which reflect the random errors and do not take into account systematic effects such as template mismatching or the presence of dust and faint emission, see below) are very small, in the range 3-7 km/s for the recessional velocities and velocity dispersion, and 0.006-0.02 for the h_3 and h_4 coefficients. They are calibrated with simulations and are determined to better than 20%. They agree with the scatter of the points except for the 5 pairs of points with $5 < R < 20$ arcsec. In this region the spectra on the two sides of the galaxy are slightly different, probably due to low level emission. The $H\alpha$ maps (Goudfrooij et al. 1994, Singh et al. 1995, Macchetto et al. 1996) show that the emission is patchy in the 10-20 arcsec region along the slit position. Dust is also present (Goudfrooij et al. 1994). Bicknell et al. (1989), who notice the same asymmetry, suggest that "old shells" might also be partly responsible. In the inner 1.5 arcsec, where σ increases to 370 km/s, there is still some template mismatching, which none of the 15 comparison stars is able to eliminate. The outermost datapoint has low signal and only the mean velocity dispersion datapoints are reliable.

Fig. 1 shows the kinematical profiles including h_3 and h_4, with the major axis data folded with respect to the center, and the spectra parallel to the minor axis folded with respect to the major axis. The rotation along the major axis is small, $\lesssim 30$ km/s, and is present also along the position parallel to the minor axis. The velocities measured in the inner 3 arcsec might indicate the presence of a kinematically decoupled core. The velocity dispersion increases to ≈ 370 km/s in the inner 5 arcsec, and flattens to ≈ 250 km/s in the outer region. The antisymmetric deviations from a Gaussian profile as parametrized by the h_3 coefficients are slightly negative where rotation is detected (see BSG94). The symmetric deviations

measured by the h_4 coefficients are smaller than 0.05 and mostly positive.

The comparison with the rotational velocities along the major axis of Bicknell et al. 1989), D'Onofrio et al. (1995), Franx et al. (1989), Graham et al. (1998) and Longo et al. (1994) is shown in the lower panel of Fig. 2. There is overall good agreement within the quoted errors. The systematic deviations observed for the outermost datapoints of Longo et al. (1994) and D'Onofrio et al. (1995) suggest that these datasets are probably affected by residual sky subtraction errors. The comparison with the dispersion profiles of Bicknell et al. (1989), D'Onofrio et al. (1995), Franx et al. (1989), Graham et al. (1998), Longo et al. (1994), Stiavelli et al. (1993), and Winsall and Freeman (1993) is shown in the upper panel of Fig. 2. There is overall agreement within the (usually large) errorbars given by the authors. Systematic differences are observed in the inner 5 arcsec, where differences in seeing and slit width may play an important role. In the outer parts the velocity dispersions of Bicknell et al. (1989) are systematically smaller than our data. However, our data agree well with Graham et al. (1998) and with the point at $R \approx 80$ arcsec measured by Winsall and Freeman (1993).

3. Dynamical modeling

The algorithm used to analyse the kinematic data presented above follows closely the technique discussed in detail by G+98. Therefore here we limit ourselves to summarizing its main features and the modifications we implemented to fit NGC 1399. In §3.1 we focus on the modeling of the light distribution; in §3.2 we concentrate on the non-parametric reconstruction of the distribution function.

3.1. The deprojection of the light distribution

The surface-brightness (SB) data of NGC 1399 consist of three sets: in the innermost part we use V-band HST-data from Lauer et al. (1995), the medium range is covered by ground-based B-band CCD-data from Bicknell et al. (1989), and the outer part by photographic V-band data from Schombert (1986). As described in Bicknell et al. (1989) we used the Schombert (1986) data shifted by 1.2 mag and from 57" on outwards. The HST-data are also shifted by 0.8 mag and are used out to 10". With an effective radius of 42" according to Faber et al. (1989) the
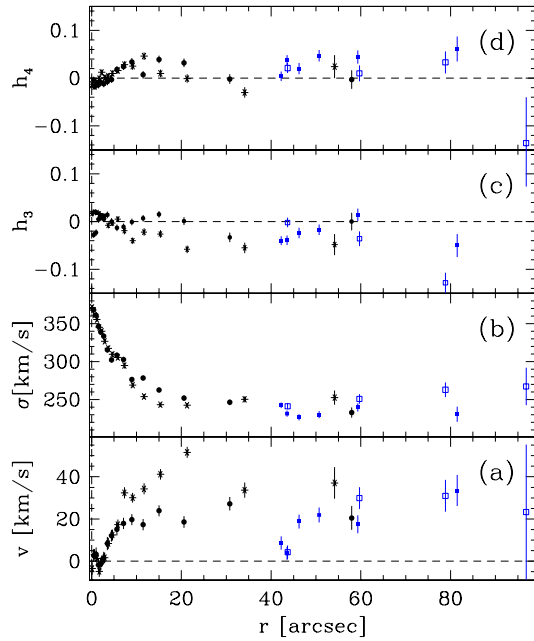
Fig. 1.— The kinematics of NGC 1399. (a) The folded mean velocity, (b) velocity dispersion, (c) h_3 and (d) h_4 profiles. Crosses and filled circles refer to the two sides of the galaxy and the major axis spectrum. Open and filled squares refer to the two sides of the galaxy and the spectra taken parallel to the minor axis and shifted 42 arcsec from the center.
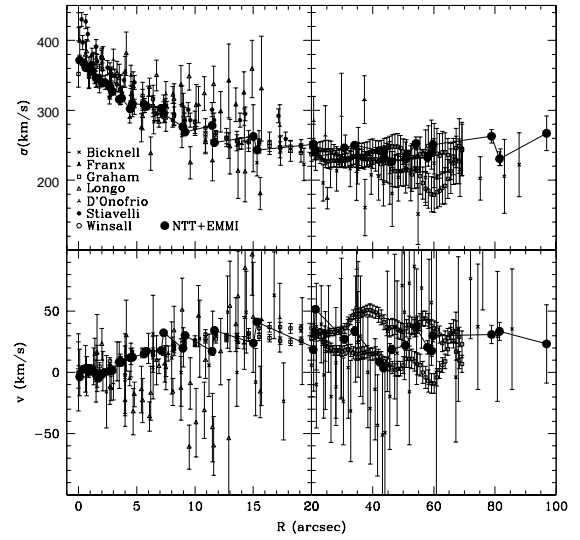

Fig. 2.— Comparison with the velocity dispersion (top) and rotation velocities (bottom) of Bicknell et al. (1989, crosses), Franx et al. (1989, triangular diamonds), Graham et al. (1998, open squares), Longo et al. (1994, open triangles), D'Onofrio et al. (1995, triangular crosses), Stiavelli et al. (1993, stars), Winsall and Freeman (1993, open circle). The line connects the data points determined here (full circles). Note the change of scale at $R = 20''$.

photometric data extend over 75 effective radii. (Note that Caon et al. 1994 find $R_e \equiv \sqrt{a_e b_e} = 127''$ by fitting their extended photometry. The determination of the total magnitude and effective radius of NGC 1399 is highly uncertain, since its light profile is very shallow in the outer regions. The exact value of R_e does not play a role in the following analysis).

The surface brightness profile deviates strongly from a de Vaucouleurs or Jaffe profile, being much brighter in the outer parts. Thus contrary to NGC 6703, for which G+98 could model the light distribution of NGC 6703 as a Jaffe (1983) profile, we must here determine the three–dimensional luminous density of NGC 1399 by deprojection.

NGC 1399 is nearly round (E0-E1). If we assume spherical symmetry the deprojection of the SB profile $\Sigma(R)$ to a spatial luminosity density $j^{lum}(r)$ is unique and is given by the standard Abel equation

$$j^{lum}(r) = -\frac{1}{\pi} \int_r^\infty \frac{d\Sigma(R)}{dR} \frac{dR}{\sqrt{R^2 - r^2}}. \qquad (1)$$

To avoid the amplification of noise, we follow Wahba and Wendelberger (1980), Scott (1990), and Gebhardt et al. (1996), and first smooth the data by finding the function $\Sigma(R)$ (expressed as thin plate splines) which maximizes the logarithm M of likelihood $\mathcal{L}$

$$M = \log\mathcal{L} = \sum_i \frac{(\log\Sigma_i - \log\Sigma(R_i))^2}{\epsilon_i^2} - \lambda P(\Sigma), \quad (2)$$

where Σ_i denotes the observed SB at projected radius R_i and ϵ_i the measurement error. The second term on the right hand side is a penalty function P (the second derivative of the SB profile $-2.5 d^2 \log\Sigma / d\log R^2$) which penalizes oscillations in $\Sigma(R_i)$ induced by noise. The factor λ controls the degree of smoothing. We fixed it to 0.003, which allows to reproduce smoothly the outer, noisy regions of the galaxy without affecting the inner, high signal to noise datapoints. We also tried using the more objective Generalized Cross Validation (GCV) method to determine the smoothing parameter, but this did not give useful results for this inhomogeneous data set.

The smoothed SB-profile is then deprojected using eq. (1). The error introduced by this inversion can be checked by generating data from a known model and deprojecting. For SB data drawn from a Jaffe-model (Jaffe 1983), with similar quality as the NGC 1399 data, the deviations between the known and the deprojected luminosity density profile are smaller than 0.5% rms. Figure 3 shows the surface brightness profile of NGC 1399 and that obtained by projecting the luminosity density model computed from our deprojection method. The differences are smaller than 0.05 mag/arcsec^2 for most of the radial range, and smaller than 0.02 mag in the integrated luminosities.

The resulting density-profile is rather shallow, with some intrinsic structure at large radii. This would be lost if we had fitted a parametrized model to the surface brightness data; by contrast the regression–inversion method described above does not smooth away intrinsic features or force the profile to a fixed asymptotic decrease in the outer parts, as is the case in many analytic models.

3.2. The distribution function

To analyse the line of sight velocity profile data we proceed in two steps (Merritt 1993, Rix et al. 1997, G+98): First, the gravitational potential is kept fixed and the best-estimate distribution function (DF) is determined, in a least–squares sense. For ideal data, the solution to this problem in the spherical case would be unique (Dejonghe and Merritt 1992). Then, this process is repeated for different gravitational potentials to determine those for which a statistically good fit to the data can be achieved with positive DF. Because changing the gravitational potential has a different effect on the line profiles than changing the anisotropy of the stellar orbits (e.g., Gerhard et al. 1998b), both can be constrained; i.e., only a limited range of potentials is consistent with the data.

The potentials examined here are the sum of the potential of the luminous matter, obtained by solving Poisson's equation for the spherical luminosity density found in §3.1, and that of a dark halo taken to be

$$\Phi^{DM} = \frac{1}{2} v_0^2 \ln\left(r^2 + r_0^2\right) \qquad (3)$$

where v_0 is the asymptotic circular velocity and r_0 the core radius of the halo. We explored models with velocities v_0 from 0 (the self-consistent model) to 780 km/s and r_0 from 0.5 to 6.0 R_e. Models with these potentials minimize the contribution of the dark halo near the center and hence maximize the mass-to-light ratio of the luminous component. In this sense they are similar to the maximum disk models for spiral galaxies; by analogy we refer to them as *maximum stellar mass models*. A priori these halo potentials might not be correct; in fact, from cosmological sim-
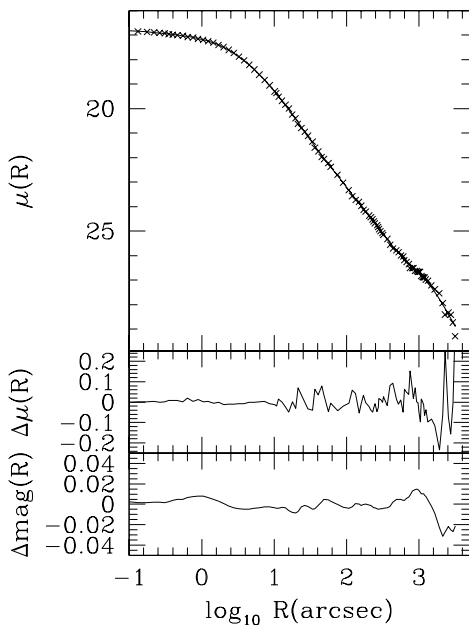
ulations (Navarro, Frenk and White 1997) one expects more centrally peaked halo distributions with asymptotic profiles at large radii $\propto r^{-3}$. However, the mass profiles derived from our approach match well the X-ray mass distribution (see Fig. 7 and §4.3). In addition, the luminous density profile derived in §3.1 is well approximated by a r^{-2} power law beyond 1".

To recover the DF of a galaxy we construct a set of basis DFs in a fixed potential. Each basis DF has a different anisotropy structure and reproduces the luminous density profile determined as in §3.1. The total DF is then a weighted sum of 57 of these basis functions:

$$f = \sum_k a_k f_k, \qquad (4)$$

with $\sum_k a_k = 1$ and the additional constraint that $\sum_k a_k f_k \geq 0$. everywhere. For the basis functions f_k we used sequences of tangentially anisotropic models as described in §4.1 and App. A of G+98 , as well as the isotropic model and a function with radially anisotropic orbital structure. The radial function is used for determining the optimal velocity scales when computing the projected Gauss-Hermite moments for each of the f_k. The coefficients a_k are determined by fitting the projected model kinematics to the I datapoints such that

$$\Delta^2 = \sum_{k=1,I} \left\{ \chi^2_{\sigma,k} + \chi^2_{2,k} + \chi^2_{4,k} \right\} + \lambda \sum_{i,j} \Lambda(f)_{i,j} \quad (5)$$

is minimal. Here χ^2_σ, χ^2_2 and χ^2_4 are as in Eqs. (8) and (9) of G+98 and measure the error-weighted square differences between the velocity dispersions of the galaxy and the model, and similarly for the second and fourth order Gauss-Hermite moments related to the measured h_4 coefficients. Following G+98 , we write the penalty function Λ as a combination of the second derivatives of the composite DF, evaluated on a grid of points (E_i, x_j) in the energy and circularity integrals. However, in the present case some care is needed in normalizing these second derivatives, to avoid that a few data points dominate the regularisation terms. For, as expected from the correlation between galaxy magnitude and the steepness of the central profile slope (Faber et al. 1997), NGC 1399 has a rather shallow central cusp. Flat density-profiles towards the center cause the distribution function to become very steep (Dehnen 1993), and similarly its second derivatives. After testing different regularization functionals on simulated data of kwown distri-

Fig. 3.— Top panel: the combined surface brightness profile μ of NGC 1399 (crosses) and the projection of the derived luminous density model (full line; see §3.1). Middle panel: the residuals $\Delta\mu$ in magnitudes per square arcsec between the observed SB profile and the model. Lower panel: the residuals Δmag in magnitudes between the integrated luminosity of NGC 1399 and the model.

bution functions, we found that the best results are obtained by setting

$$\Lambda(f) = \frac{1}{(f''_{\text{iso}})^2} \left(\frac{\partial^2 f}{\partial E^2} \right)^2 + \frac{2}{(f'_{\text{iso}})^2} \left(\frac{\partial^2 f}{\partial E \partial x} \right)^2 + \frac{1}{(f_{\text{iso}})^2} \left(\frac{\partial^2 f}{\partial x^2} \right)^2 , \quad (6)$$

where f_{iso}, f'_{iso} f''_{iso} are the isotropic distribution function and its first and second derivative with respect to energy.

The value of λ in Eq. 5 determines the degree of smoothness of the composite DF. Low values of λ result in a perfect fit to the data at the price of unphysical small–scale variations in the DF. Large values of λ produce very smooth DFs which might not give acceptable fits to the data. We estimate the optimal value of λ by considering the composite DF recovered from Monte Carlo simulated data, which are derived from an underlying distribution function similar to the one that gives the best fit to the NGC 1399 data, with the assumption of Gaussian errors (see G+98 for details). Fig. 4 shows the normalized total χ^2 of the fit to the artificial data and the percentage rms variations of the recovered DF, averaged over 25 realizations, as a function of λ. A potential with only the luminous matter and one including a halo with $r_0 = 168$ arcsec, $v_0 = 427$ km/s are used for Fig. 4. In both cases values around $\lambda \approx 0.01$ give $\chi^2 \approx 1$ and less than 15% mean rms variations of the DF. In the analysis of NGC 1399 we thus adopt $\lambda = 0.02$. Note that in G+98 we found that slightly different values of λ were needed to fit the self-consistent and the halo potential cases. The difference here stems from the dominant role of the luminous component in NGC 1399 (see §4.3).

Finally, we constructed cumulative χ^2 distributions for sets of 100 Monte Carlo simulations of our data set, drawn from radial and tangential models in self-consistent or halo potentials, respectively, and analyzed using $\lambda = 0.02$. We find that the 95% confidence level is reached at a value of $\chi^2 \approx 1.3$ per data point in all these cases. The same value results also when all errors are increased by 25%, with $\lambda = 0.02$ still beeing the optimal smoothing parameter. If we increase all errors by 40%, the 95% confidence level is reached at a value of $\chi^2 \approx 1.37$ per data point.

4. Results

4.1. Stellar kinematics

As discussed in §2, the kinematic data show differences between the two sides of the galaxy significantly
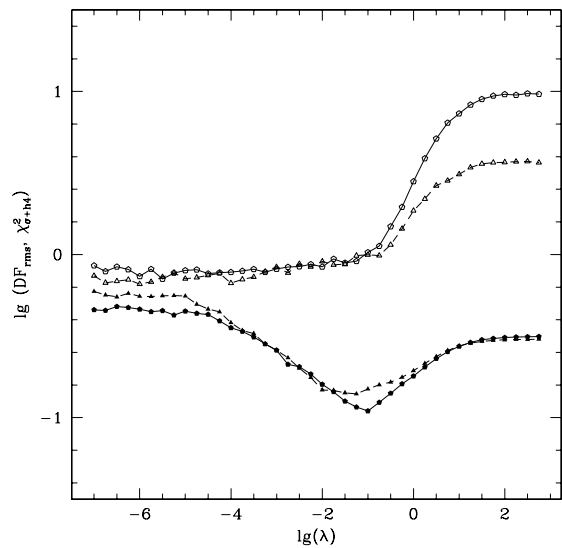

Fig. 4.— Model results as a function of the regularization parameter λ. The upper two curves show the total χ^2 per σ and h_4 data point of regularized composite models with 57 basis functions. The lower curves show the rms deviation between the recovered composite model distribution function and the true distribution function from which the data sets were generated. This rms deviation was evaluated on a grid in energy and angular momentum corresponding to radii < 3 times the radius of the outermost data point. Triangles refer to the self-consistent model, pentagons to a model in a halo potential with $r_0 = 168$ arcsec and $v_0 = 427$ km/s.

larger than the (small) statistical errors, probably due to low–level patchy emission. For radii $10 < |R| < 22$ arcsec, we therefore use in the following the average values of σ and h_4 over the two sides, adopting as errors half of the side–to–side differences. In addition, while minimizing the square differences between models and datapoints over the whole radial range, we quote χ^2 values computed only from points at $|R| > 5$ arcsec. The velocity dispersion of NGC 1399 steeply increases to 370 km/s in the central 5 arcsec, which probably indicates the presence of a central massive object (Stiavelli et al. 1993). We explore models with central black holes at the end of this section.

The full line in Fig. 5 shows a dynamical model that best fits the kinematic data, obtained with a dark halo potential with $r_0 = 210$ arcsec, $v_0 = 323$ km/s, corresponding to a total circular velocity $V_{\rm circ} = 383$ km/s at the last data points, $R = 97''$. Fits of similar quality are obtained for a small range of model potentials; see the discussion in G+98. Fig. 5 shows three other models that span this range in the present case. These have circular velocities at the last data point of $V_{\rm circ} = 404, 425, 442$ km/s, respectively. All these models represent the data very well, with rms differences in σ of about 10 km/s, or 4.4 %, and in h_4 of about 0.018 (excluding the last datapoint). The dotted line in the figure shows the best model without dark halo ($V_{\rm circ} = 364$ km/s); this has similar rms differences in σ and h_4 when only datapoints within 60 arcsec are considered, but substantially larger values, 19 km/s, or 8.7% rms in σ, and 0.027 rms in h_4, when the datapoints at $R > 60''$ are included. Therefore we conclude that the gravitational potential of the galaxy in the region probed by the absorption line data is dominated by the luminous component, but that the influence of the dark component is marginally detected starting at $R \approx 60''$.

Despite the excellent fit, the statistical interpretation of the resulting χ^2 values is not straightforward. The top panel of Fig. 6 shows the values of the normalized global $\chi^2_{\sigma + h_4}$ obtained for the model fits, as a function of the circular velocity of the model at the last datapoint, $R = 97''$. Best-fit models are found in the range $380 < V_{\rm circ} < 450$ km/s with values $\chi^2_{\sigma + h_4} \approx 1.9$, while the self-consistent model gives $\chi^2_{\sigma + h_4} \approx 3.7$. The Monte Carlo simulations of our data shown in Fig. 4 demonstrate that the employed set of basis functions is sufficient to produce $\chi^2 \approx 1$, for a Gaussian error distribution and when the underlying model distribution function is similar to NGC

1399 and smooth. In these simulations the 95% confidence limit corresponds to $\chi^2 \approx 1.3$. The rather high χ^2 values obtained for the real dataset might partly be caused by an underestimation of the error bars. Fitting to the data for NGC 1399 with all errorbars increased by 25% gives a normalized $\chi^2 = 1.3$ for our best–fitting model, just marginally acceptable in a statistical sense (see above). Only when all errorbars are increased by 40% is the fitted model's χ^2 reduced to 1.06. However, the (statistical) uncertainty of the Monte Carlo–estimated error bars is not larger than 20% (see §2), so most of the large χ^2 must be due to systematic effects.

Smaller, but still greater than unity, values of χ^2 are obtained if the two sides of the galaxies are fit separately ($\chi^2 = 1.19$ and 1.58 for the two sides, using the original errors). This indicates that the systematic differences between the two sides discussed in §2 are playing an important role. Also important are sudden point–to–point variations in the measured data values which are unlikely to be physical. We conclude that the residual differences (at the two-three percent level) between model and data are of a systematic nature, with the most obvious candidates being dust, unresolved emission, local template mismatch, and slight oversmoothing of the model. This also suggests that we might have reached the intrinsic precision limit of stellar absorption line measurements.

To estimate confidence intervals for the potential parameters, we therefore proceed as follows. We assume that due to systematic effects the real errors on our kinematic data points are 40% larger than the statistical errors determined from Monte Carlo simulations, so that the best-fitting model has a $\chi^2 \simeq 1$ per data point (the number of degrees of freedom is only slightly smaller than the number of data points due to the enforced regularization). The 95% confidence line is then at $\chi^2 = 1.37 \times 1.4^2 = 2.68$ in units of the original errors; see Figure 6, top panel. The resulting 95% confidence range for the circular velocity at $R = 97''$ is $V_{\rm circ} = 420 \pm 40$ km/s. This is consistent with the sharp increase of the minimum values of χ^2 seen for $V_{\rm circ} < 380$ km/s and $V_{\rm circ} > 450$ km/s, which clearly indicates that this procedure gives a fair estimate for the range of allowed circular velocities for the combined luminous matter and halo potential. In this sense the four halo models shown in Fig. 5 bracket the range of acceptable models.

The bottom panel of Fig. 5 shows the anisotropy

profiles derived for the different potentials discussed above. As a general trend, the profiles favour values of $\beta \approx 0.3$. The maximum at 10" and sharp drop in the inner 5 arcsec is uncertain (see discussion below), while the tendency of the most massive models to become tangentially anisotropic in the outer parts is also uncertain until confirmed by data at still larger radii; see §4.2 and the discussion in G+98 . We conclude that NGC 1399 is slightly radially anisotropic with $\beta = 0.3 \pm 0.1$ out to $R = 60$ arcsec or 5 kpc; and that the anisotropy is not yet well–constrained at larger radii. This is similar to what was found for NGC 6703 (G+98) and NGC 2434 (Rix et al. 1997).

Finally, we briefly investigate the influence of the possible presence of a massive black hole on the inferred anisotropy in the center, without attempting a detailed analysis (this will be worthwhile only for data with HST resolution). We construct models with a central black hole of mass around $M = 5 \times 10^8 M_\odot$, which is approximately the mass expected for a galaxy of the luminosity of NGC 1399 (van der Marel 1999). We find that in these models the fit to the velocity dispersion profile in the inner 5 arcsec follows the steep increase of the measured σ better, and the anisotropy change is milder. In models with massive black holes the inferred anisotropy can be substantially changed even at $10''$, and is slightly reduced at $\sim 20''$.

4.2. The Globular Cluster and Planetary Nebulae systems

The mass distribution of NGC 1399 can be constrained further by considering its globular cluster (GC) and planetary nebulae (PN) systems. Grillmair et al. (1994), Minniti et al. (1998) and Kissler-Patig et al. (1998) measured the radial velocities of 74 GCs, with typical errors of 100 km/s. Forbes et al. (1998) studied the radial distribution of the GCs and found that their surface density profile is flatter than the galaxy starlight, following a power law of slope $\gamma \approx -1.47$, 0.28 dex shallower than the galaxy. Thus at the same radius we expect the GCs to have a velocity dispersion $\sim (1.75/1.47)^{1/2} \approx 1.08$ larger than the stars of NGC 1399 (see, e.g., Binney and Tremaine 1987), assuming a logarithmic potential and a nearly isotropic distribution function for both components, which for the stars is approximately the case. The discussion below does not change if we ignore this small correction.

Arnaboldi et al. (1994) measured the radial velocities of 37 PNs, with typical errors of 50 km/s. The
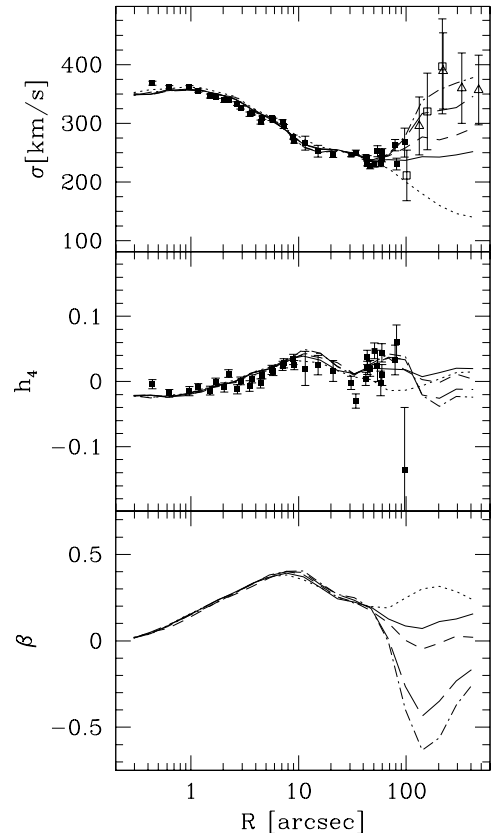

Fig. 5.— Dynamical models for the kinematics of NGC 1399 in several luminous plus dark matter potentials, compared to the measured projected velocity dispersion (top panel) and velocity profile shape parameter h_4 (middle panel). Full, dashed, long-dashed, dot-dashed lines: best-fit models with $V_{\rm circ} = 383, 404, 425, 442$ km/s at $R = 97''$ respectively. Dotted lines: self–consistent model with luminous matter only, $V_{\rm circ} = 364$ km/s. Filled squares refer to the stellar kinematics, open squares are the velocity dispersions derived for globular clusters, reduced by the factor 1.08 (see §4.2). The open triangles are the velocity dispersions derived from planetary nebulae velocities. The bottom panel shows the models' intrinsic anisotropy parameter $\beta(r)$.

9

intrinsic density distribution of the PNs is not as well established as for the GCs. We assume that in the outer parts of NGC 1399 the density distribution of PNs follows that of the stars, with the same velocity dispersion. This is consistent with the histogram shown in McMillian, Ciardullo and Jacoby (1993), but the number of PNs used is small and there is a possible selection bias from the coupled effects of the metallicity dependence of the specific density of PNs (Ciardullo and Jacoby 1992) and the observed color gradients in elliptical galaxies (Richer, McCall, Arimoto 1997). Fig. 5 shows the velocity dispersions (with their statistical errors) derived by binning radially the GC and PN velocities.

We proceed to compute the likelihood of the two datasets on our grid of gravitational potentials as follows. For each model we take the projected velocity dispersion profile $\sigma(R)$, as determined in §4.1, and approximate the probability for measuring a given line–of–sight velocity at radius R_i by a Gaussian of zero mean and rms= $f\sigma(R_i)$, where $f = 1.08$ for the comparison with the GCs and $f = 1$ for the PNs. This simplifying assumption is justified by the low number of GCs and PNs velocities available and their rather large errors. Monte Carlo simulations showed that deviations from Gaussians can be detected only with samples of more than a few hundred measured velocities; see also Merritt (1997). After convolution with the (Gaussian) error distribution specified by the respective σ_i of each data point, we write the likelihood of the set of measured radial velocities v_i as

$$\mathcal{L}_{GC} = \Pi_{i=1}^{74} \frac{1}{\sqrt{2\pi[f^2\sigma^2(R_i) + \sigma_i^2]}} \exp\left(-\frac{v_i^2}{2[f^2\sigma^2(R_i) + \sigma_i^2]}\right), \quad (7)$$

and similarly for $\mathcal{L}_{PN}$. For comparison we also compute the likelihoods $\mathcal{L}_{MC}$ of simulated sets of GC and PN radial velocities, generated from our best-fit model of NGC 1399.

The middle and bottom panels of Fig. 6 show the results. Here we plot as a function of the circular velocity at $R = 97''$ the likelihoods of the models. Additionally, we show two lines. The dotted line displays the mean value of the likelihood $-\ln \mathcal{L}$ for 100 Monte Carlo realizations of $N = 74$ GCs with velocities drawn from the projected kinematics of one of our best fitting models (-547.6), and the same quantity (-266.45) for $N = 37$ PNs. The dashed line gives the 95% confidence level below which only 5% of the Monte Carlo realizations fall, for the GC (-

553.9) and the PN (-272.5) samples. It is seen that the GCs and PNs favour the high mass halo models of the range compatible with the absorption line data, and are inconsistent with the self–consistent model. The models that are best for the GC sample have $-\ln \mathcal{L}_{GC} \approx -547$; they therefore give a good representation of the available data set. The same is true for the PN set. For both the GCs and the PNs, $\mathcal{L}_{PN}$ decreases sharply for models with $V_{\mathrm{circ}} < 380$ km/s, in agreement with the results of §4.1. The Monte Carlo simulations quoted above rule out the self-consistent model to almost certainty with either the GC or the PN sample. However, models with more massive halos than allowed by the stellar kinematics are compatible with the GC and PN data.

We have estimated the effect of a possible contamination of the GC and PN samples by intracluster objects. As suggested by Theuns and Warren (1997) and Mendez et al. (1997), some of the GCs and PNs considered above could in fact be foreground or background objects in the Fornax Cluster but not associated with NGC 1399. To test the sensitivity of our results to such a contamination, we repeat the analysis on a subset of GCs and PNs where the 10 or 20 percent objects with the highest relative velocities have been eliminated. This is an extreme case, since we might expect some of the contaminors to have smaller velocities. We find that the results derived for the GC set are rather robust, with the best-fit potential remaining within the error range given above. However, when considering the PNs without the 8 fastest objects dark halos with circular velocities as low as $V_{circ} \approx 350$ km/s are allowed. Velocities $V_{circ} > 550$ km/s are also less favoured.

4.3. The mass and M/L distribution

Fig. 7 shows the permitted range for the cumulative mass distribution in NGC 1399, as derived from our combined fits to the absorption line kinematics and the radial velocities of GCs and PNs. The dark matter contribution is negligible for $R \leq 60$ arcsec or 5 kpc and becomes progressively dominant at larger R. It comprises at most 1/3 of the total mass at the last stellar kinematic data point, $R = 97''$ or 8 kpc, and 1-3 times the luminous mass at the radius of the most distant GC with a measured radial velocity, $R \approx 417$ arcsec or 35 kpc. Inside this radius, the allowed mass range matches the profiles derived from X-ray data by modeling the cooling flow (Ikebe et al. 1996), giving $M = 1.2-2.5\times10^{12}M_\odot$. At larger radii
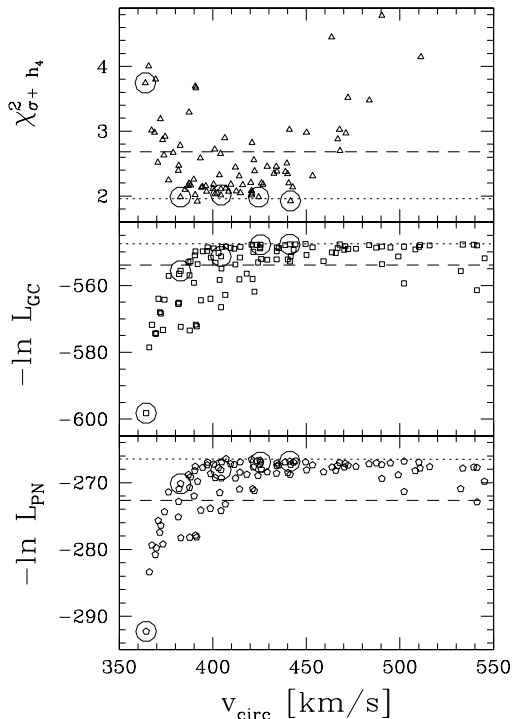
10

Fig. 6.— Quality of the kinematic model fits for NGC 1399 as a function of the true circular velocity at $R = 97''$. Top: the normalized χ^2 of the fit to the $\sigma - h_4$ datapoints. The dotted line shows the mean χ^2 (scaled to the real errors) of the best-models obtained from Monte Carlo simulations, when the errors are increased by 40% (see text). The dashed lines show the related 95% level, indicating an allowed range of $V_{\text{circ}} = 420 \pm 40$ km/s. Middle: the likelihood $-\ln \mathcal{L}_{GC}$ of the Globular Cluster dataset. Bottom: the likelihood $-\ln \mathcal{L}_{PN}$ of the Planetary Nebulae dataset. The models shown in Fig. 5 are circled. The dotted lines show the mean likelihood of the best-models obtained from Monte Carlo simulations. The dashed lines show the 95% level.

our simple models based on logarithmic halo potentials fail to follow the knee inferred from the X-ray data, which Ikebe et al. (1996) interpret as the transition of the galaxy potential to the Fornax cluster potential. Neverless these simple mass profiles are on the right mass scale even at these large distances.

The integrated mass-to-light ratio in the B band is approximately constant at $M/L_B \approx 10 M_\odot/L_\odot$ out to $R \approx 60''$, increases to 12-15 at $R \approx 97''$ and reaches $M/L_B = 22 - 48 \ M_\odot/L_\odot$ at $R = 417''$. Old ($t \geq 8$ Gyrs) and metal rich ($Z \geq Z_\odot$) stellar populations (Worthey 1994) can provide $M/L_B \approx 10$, matching at the same time the values of the Mg_2 index and $(B - V)$ color observed in the central regions of NGC 1399 ($Mg_2 = 0.334$, $(B - V) = 0.99$, Faber et al. 1989).

5. Conclusions

We have presented new accurate and extended stellar kinematic data for NGC 1399, the cD galaxy of the Fornax cluster. Using a non-parametric algorithm, we have constructed smooth (at the 15 % level) spherical distribution functions which reproduce the observed velocity dispersion and h_4 profiles at the four percent level. The models were tested for a grid of gravitational potentials, which combine a luminous part obtained from the deprojected surface brightness distribution with the assumption of constant M/L, and a quasi–isothermal logarithmic dark halo potential. We have also explored the influence of a central black hole of mass $5 \times 10^8 M_\odot$, finding that the steep increase in σ in the inner 5 arcsec can be better followed. We have further constrained the mass profile of the galaxy by taking into account the likelihoods of the radial velocities measured for the galaxy's globular cluster and planetary nebulae systems and by comparing the results with the potential derived from X-ray measurements. Our main conclusions are summarized as follows:

1. The stellar orbital structure of NGC 1399 is moderately radial out to $R \approx 60''$, with $\beta = 0.3 \pm 0.1$, and is not yet well–constrained at larger radii by the presently available data.

2. The luminous component of the galaxy dominates the dynamics out to $R \approx 60''$, with $M/L_B = 10 M_\odot/L_\odot$. Old and metal rich stellar populations reproduce this high value, matching also the measured values of the central $(B - V)$
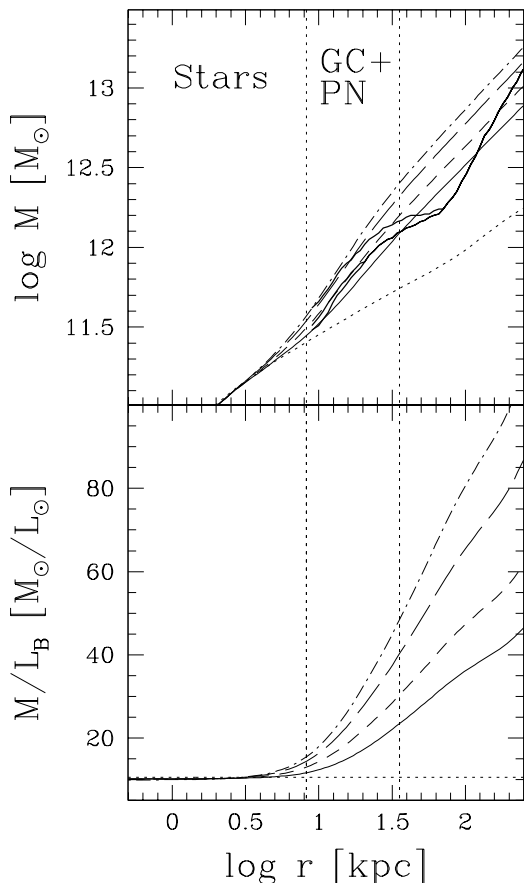
11

Fig. 7.— Top: the total mass as a function of radius for the range of acceptable models for NGC 1399. Bottom: the mass to light ratio in the B band. Line styles as in Fig. 5. The full thick lines show the mass profiles derived from X-ray observations (see §4.3).

color and Mg_2 index.

3. The influence of the dark halo is detected around $R \approx 60 - 90''$ and becomes dominant in the region probed by the GC and PN systems, where the self-consistent model is ruled out.

4. The circular velocity at the last measured stellar kinematic point is $V_{\rm circ} = 380 - 450$ km/s. The corresponding mass profile range matches the mass curves derived from X-ray data with different assumptions to model the galaxy's cooling flow. Inside $R = 417''$ or 35 kpc we derive $M = 1.2 - 2.5 \times 10^{12} M_\odot$ and a cumulative $M/L_B = 22 - 48 \ M_\odot/L_\odot$.

5. The kinematics of the GCs and the PNs are consistent with those of the stars within the large statistical errors. The GCs appear slightly hotter, even when a correction for the different density profile slope is taken into account.

When compared to the normal giant ellipticals where a detailed stellar dynamical analysis has been performed (NGC 1600, Matthias and Gerhard 1999; NGC 2434, Rix et al. 1997 ; NGC 6703, G+98), the cD galaxy NGC 1399 appears to have a similar anisotropy profile inside the inner few kiloparsecs, with $\beta \approx 0.3$. The luminous component of the galaxy dominates the gravitational potential out to 8 kpc from the center. As judged from the GC and PN data, the transition to the dark matter dominated regime appears to be more rapid than in the case of NGC 6703. It is possible that this difference reflects the special position of NGC 1399 at the center of the Fornax cluster. The best way to derive more stringent constraints on the nature of the transition region appears to be from larger samples of PN velocities such as can be obtained with the VLT and other large telescopes.

The present analysis based on spherical models is adequate to study the very round inner regions of NGC 1399 considered here. For more flattened systems the methods developed by Matthias and Gerhard (1999) and Cretton et al. (1999) are the future ways to follow.

REFERENCES

Arnaboldi, M., Freeman, K.C., Hui, X., Capaccioli, M., Ford, H., 1994, The Messenger 76, 40

Arnaboldi, M., Freeman, K.C., Gerhard, O.E., Matthias, M., et al., 1998, ApJ, 507, 759

Bender, R., 1990, A&A, 229, 441

Bender, R., Saglia, R.P., Gerhard, O., 1994, MNRAS, 269, 785 (BSG94)

Bicknell, G.V., Bruce, T.E.G., Carter, D., Killeen, N.E.B., 1989, ApJ, 336, 639

Binney, J., Tremaine, S. 1987, Galactic Dynamics (Princeton: Princeton Univ. Press)

Caon, N., Capaccioli, M., D'Onofrio, M., 1994, A&AS, 106, 199

Carollo, C.M., de Zeeuw, P.T., van der Marel, R.P., Danziger, I.J., Qian, E.E., 1995, ApJ 441, L25

Ciardullo, R., Jacoby, G.H., 1992, ApJ, 388, 268

Cohen, J.G., Ryzhov, A., 1997, ApJ, 486, 230

Cretton, N., de Zeeuw P.T., van der Marel, R.P., Rix, H.-W., 1999, ApJ, submitted, astro-ph/9902034

Dehnen, W., 1993, MNRAS, 265, 250

Dejonghe, H., Merritt, D., 1992, ApJ, 391, 531

D'Onofrio, M., Zaggia, S.R., Longo, G., Caon, N., Capaccioli, M., 1995, A&A, 296, 319

Faber, S., Wegner, G., Burstein, D., Davies, R.L., Dressler, A., Lynden-Bell, D., Terlevich, R., 1989, ApJS, 69, 763

Faber, S.M., Tremaine, S., Ajhar, E., Byun, Y.-I., Dressler, A., Gebhardt, K., Grillmair, C., Kormendy, J., Lauer, T., Richstone, D. 1997, AJ, 114, 1771

Forbes, D.A., Grillmair, C.J., Willinger, G.M., Elson, R.A.W., Brodie, J.P., 1998, MNRAS, 293, 325

Franx, M., Illingworth, G., Heckman, T., 1989, ApJ, 344, 613

Gebhardt, K., et al., 1996, AJ, 112, 105

Geiger, B., Schneider, P., 1998, MNRAS, 302, 118

Gerhard, O.E., 1993, MNRAS, 265, 213

Gerhard, O.E., Jeske, G., Saglia, R.P., Bender, R., 1998a, MNRAS, 295, 197 (G+98)

Gerhard, O.E., Jeske, G., Saglia, R.P., Bender, R., 1998b, in Galactic Halos, ASP Conf. Ser. Vol. 136, ed. Zaritsky, D., ASP, San Francisco, 248

Goudfrooij, P., Hansen, L., Jørgensen, H.E., Nørgaard-Nielsen, H.U., 1994, A&AS, 105, 341

Graham, A., Colless, M.M., Busarello, G., Zaggia, S., Longo, G., 1998, A&AS, 133, 325

Graham, A., Colless, M., Busarello, G., 1998, ASP 136, 257

Grillmair, C.J., Freeman, K.C., Bicknell, G.V., Carter, D., Couch, W.J., Sommer-Larsen, J., Taylor, K., 1994, ApJ, 422, L9

Hui, X., Ford, H.C., Freeman, K., Dopita, M.A., 1995, ApJ, 449, 592

Ikebe, Y., Ezawa, H., Fukazawa, Y., Hirayama, M., Ishisaki, Y., Kikuchi, K., Kubo, H., Makishima, K., Matsushita, K., Ohashi, T., Takahashi, T., Tamura, T., 1996, Nature, 379, 427

Jaffe, W., 1983, MNRAS, 202, 995

Jones, C., Stern, C., Forman, W., Breen, J., David, L., Tucker, W., Franx, M., 1997, 482, 143

Kissler-Patig, M., Brodie, J.P., Schroder, L.L., Forbes, D. A., Grillmair, C.J., Huchra, J.P., 1998, ApJ, 115, 105

Kronawitter, A., Gerhard, O., Saglia, R.P., Bender, R., 1999, "Dynamical analysis of elliptical galaxy halos", Proc. of the Conference "Galaxy dynamics", August 1998, Rutgers, ASP, in press

Lauer, T., Ajhar, E., Byun, Y., Dressler, A., Faber, S., Grillmair, C., Kormendy, J., Richstone, D., Tremaine, S., 1995, ApJ, 110, 2622

Longo, G., Zaggia, S.R., Busarello, G., Richter, G., 1994, A&AS, 105, 433

Macchetto, F., Pastoriza, M., Caon, N., Sparks, W.B., Giavalisco, M., Bender, R., Capaccioli, M., 1996, A&AS, 120, 463

Matthias, M., Gerhard, O. E. 1999, MNRAS, in press (astro-ph/9901036)

McMillian, R., Ciradullo, R., Jacoby, G.H., 1993, ApJ, 416, 62

Mendez, R.H., Guerrero, M.A., Freeman, K.C., Arnaboldi, M., Kudritzki, R.P., Hopp, U., Capaccioli, M., Ford, H., 1997, ApJ, 491, L23

Merritt, D., 1993, ApJ, 413, 79

Merritt, D., 1997, AJ, 114, 228

Minniti, D., Kissler-Patig, M., Goudfrooij, P., Meylan, G., 1998, ApJ, 115, 121

Mould, J., Oke, J.B., de Zeeuw, P.T., Nemec, J.M., 1990, AJ, 99, 1823

Navarro, J.F., Frenk, C.S., White, S.D.M., 1997, ApJ, 490, 493

Rangarajan, F.V.N., Fabian, A.C., Forman, W.R., Jones, C., 1995, MNRAS, 272, 665

Richer, M.G., McCall, M.L, Arimoto, N., 1997, A&AS, 122, 215

Rix, H.-W., de Zeeuw, P.T., Cretton, N., van der Marel, R., Carollo, M.C., 1997, ApJ, 488, 702

Romanowsky, A.J., Kochaneck, C.S., 1999, ApJ, 516, 18

Saglia, R.P., Bertin, G., Stiavelli, M., 1992, ApJ 384, 433

Saglia, R.P., Bertin, G., Bertola, F., Danziger, I.J., Dejonghe, H., Sadler, E.M., Stiavelli, M., de Zeeuw, T., Zeilinger, W.W., 1993, ApJ, 403, 567

Saglia, R.P., 1996, Proc. of the IAU 171 Symposium "New light on Galaxy Evolution", Heidelberg, Germany, R. Bender, R.L. Davies Eds, p. 157

Schombert, J.M., 1986, ApJS, 60, 603

Schwarzschild, M., 1979, ApJ, 232, 236

Scott, D.W., 1990, Multivariate Density Function, Wiley & Sons, New York

Singh K.P., Bhat P.N., Prabbu T.P., Kembhavi A.K., 1995, A&A, 302, 658

Statler, T.S., Smecker-Hane, T., 1999, AJ, 117, 839

Stiavelli, M., Møller, P., Zeilinger, W.W., 1993, A&A, 277, 421

Theuns, T., Warren, S.J., 1997, MNRAS, 284, L11

van der Marel, R., Franx, M., 1993, ApJ, 407, 525

van der Marel, R., 1999, Proceedings of the Conference "Galaxy Dynamics", D. Merritt, M. Valluri, J. Sellwood, Eds., August 1998, Rutgers, ASP in press, astro-ph/9811025

Wahba, G., Wendelberger, J., 1980, Monthly Weather Review, 108, 1122

Winsall, M.L, Freeman, K.C., 1993, A&A, 268, 443

Worthey, G. 1994, ApJSS, 95, 107